Nanostructured Metallic Glass in a Highly Upgraded Energy State Contributing to Efficient Catalytic Performance

Chaoqun Pei, Shuangqin Chen,* Tianchen Zhao, Mai Li, Zhaotao Cui, Baoan Sun,* Sigui Hu, Si Lan, Horst Hahn, and Tao Feng*

Metallic glasses (MGs), with high density of low coordination sites and high Gibbs free energy state, are novel promising and competitive candidates in the family of electrochemical catalysts. However, it remains a grand challenge to modify the properties of MGs by control of the disordered atomic structure. Recently, nanostructured metallic glasses (NGs), consisting of amorphous nanometer-sized grains connected by amorphous interfaces, have been reported to exhibit tunable properties compared to the MGs with identical chemical composition. Here, it is demonstrated that electrodeposited Ni–P NG is characterized by an extremely high energy state due to its heterogeneous structure, which significantly promotes the catalytic performance. Moreover, the Ni–P NG with a heterogeneous structure is a perfect precursor for the fabrication of unique honey-like nanoporous structure, which displays superior catalytic performance in the urea oxidation reaction (UOR). Specifically, modified Ni–P NG requires a potential of mere 1.36 V at 10 mA cm^{-2}, with a Tafel slope of 13 mV dec^{-1}, which is the best UOR performance in Ni-based alloys. The present work demonstrates that the nanostructurization of MGs provides a universal and effective pathway to upgrade the energy state of MGs for the design of high-performance catalysts in energy conversion.

1. Introduction

Metallic glasses (MGs), known as metallic alloys with amorphous structure, have been shown to possess unique thermodynamic,[1] kinetic,[2] mechanical,[3] and magnetic[4] properties that do not exist in the crystalline counterparts. Recently, as part of the continuous exploration of the rapidly growing field of materials for energy applications, MGs have been reported to exhibit excellent catalytic performance due to their disordered structure.[5–8] For example, Ni-based MGs were reported as effective electrocatalysts used in water splitting because of their excellent performance in the oxygen evolution reaction (OER).[5–7] Fe-based MGs were reported to be particularly beneficial as advanced oxidation processes' catalysts in wastewater remediation.[9,10] It is well established that the catalytic performance is closely related to the density of active sites. Inhomogeneities in crystalline materials could play a key role in improving the catalytic performance via varying their chemical and/or defect microstructures,[11] which contributes to an increase of the density of active sites.[12,13] However, for MGs, which typically have a homogeneous disordered structure, i.e., no compositional variations, no defects as in crystalline materials, it remains a great challenge to adjust the properties of MGs for practical applications by the introduction of inhomogeneity in the disordered structure.

Additionally, the energy state (especially in terms of the surface energy) of the materials plays a vital role in the catalytic performance, with the higher surface energy possessing the higher activity, attributed to the larger number of low-coordinated sites on the surface of the catalyst.[14–18] The catalytically active sites are usually constituted of a few low-coordinated atoms on steps, edges, and kinks.[19–21] MGs are generally formed by rapid-quenching from the melt and has higher enthalpy and higher specific volume relative to the crystalline state.[22] Therefore, MGs stay in a higher energy state and possess higher density of low coordinated sites comparing to their crystalline counterparts. These merits endow MGs with superior catalytic performance, due to the low activated energy and rich of potential active sites.[23–25] A strong interest remains whether the energy state of MGs can be tuned further by

C. Pei, S. Chen, T. Zhao, M. Li, Z. Cui, S. Lan, H. Hahn, T. Feng
Herbert Gleiter Institute of Nanoscience
School of Material Science and Engineering
Nanjing University of Science and Technology
Nanjing 210094, China
E-mail: chensq-hgi@njust.edu.cn; tao.feng@njust.edu.cn
B. Sun
Institute of Physics
Chinese Academy of Sciences
Beijing 100190, China
E-mail: sunba@iphy.ac.cn
B. Sun, S. Hu
Songshan Lake Materials Laboratory
Dongguan, Guangdong 523808, China
H. Hahn
Institute of Nanotechnology
Karlsruhe Institute of Technology
76021 Karlsruhe, Germany

**ADVANCED
SCIENCE NEWS**

www.advancedsciencenews.com

**ADVANCED
MATERIALS**

www.advmat.de

modifications of the processing routes. One option to obtain the higher-energy MGs is faster and faster quenching from the molten state to the undercooled liquid to capture the higher energy state in liquid.[26] Various post-treatment processes to rejuvenate the MGs to higher energy state, such as cryogenic thermal cycling[27,28] or high-pressure treatment,[29,30] provide additional options, which have been explored extensively. These options face several problems due to the complex processing and, associated with that, large energy consumption. Therefore, the challenge remains to design and fabricate MGs with high energy state and excellent catalytic performance.

To address this challenge, novel MGs with unique structural features have been developed, which have been named nanostructured metallic glasses or nanoglasses (NGs) due to their nanometer-sized inhomogeneous structure.[5,31,32] In the structural model, NGs consist of amorphous nanometer-sized grains connected by amorphous interfaces (called glass/glass interfaces), and the glass/glass interfaces are several nanometers wide with a locally reduced density relative to the adjacent grains, which introduce significant structural heterogeneities and low coordinated sites in NGs. [32,33] Therefore, it is possible to control the properties of NGs by varying their chemical and/or defect microstructures. In addition, it has been shown that the interfaces in NGs exhibit an amorphous structure with low density, which is distinctly different from the amorphous structure of the rapidly quenched MGs. Recently, our group has shown that NGs exhibit promoted β-relaxation and enhanced microscale tensile plasticity over the MGs with the same composition, which may be associated with higher energy state.[34] However, the energy state of NGs has not been directly investigated. Furthermore, research on catalytic properties of NGs has been rarely reported up to now.[35] The initial demonstration of improved catalytic properties might trigger intensive research in this field.

Herein, Ni–P NGs with heterogeneous microstructure were prepared and their extremely high energy state compared to the conventionally prepared MG with identical composition was substantiated for the first time. The Ni–P NGs show a comprehensively improved catalytic performance in water-splitting, including the urea oxidation reaction (UOR),[36–38] the OER,[39–41] and the hydrogen evolution reaction (HER).[42–44] Moreover, it is shown that Ni–P NGs with heterogeneous microstructure are perfect starting structure for the fabrication of unique honey-like nanoporous structures, which display a superior catalytic performance in the UOR. The present work provides a universal and facile approach to synthesize high-energy MGs by nanostructurization to obtain highly efficient catalytic materials for applications in the field of clean energy.

2. Results and Discussion

The differences between the structures of the Ni–P NGs and the MGs, experimental results and the derived structural models are shown in **Figure 1**. As pointed out in previous work on NGs, the main feature of NGs is the existence of amorphous/amorphous interfaces in NGs schematically shown in Figure 1a for NG in comparison to the homogeneous structure shown in 1d. This unique heterogeneous structure of Ni–P NGs can be clearly revealed using high-resolution transmission electron microscopy (HRTEM) as shown in Figure 1b, where two different amorphous regions can be distinguished, the nanometer-sized grains region I (orange circle) and the interfacial region II (blue circle). The corresponding fast Fourier transformation (FFT) patterns of these two regions are displayed on the top right in Figure 1b, clearly indicating that both regions (nanoscaled grain and interface) are amorphous. In contrast, the HRTEM image of the Ni–P MG shown in Figure 1e clearly demonstrates the homogeneous amorphous microstructure of MG. The corresponding selected-area electron diffraction (SAED) patterns (Figure 1c,f) provide proof that both Ni–P NGs and MGs are fully amorphous, which is fully consistent with
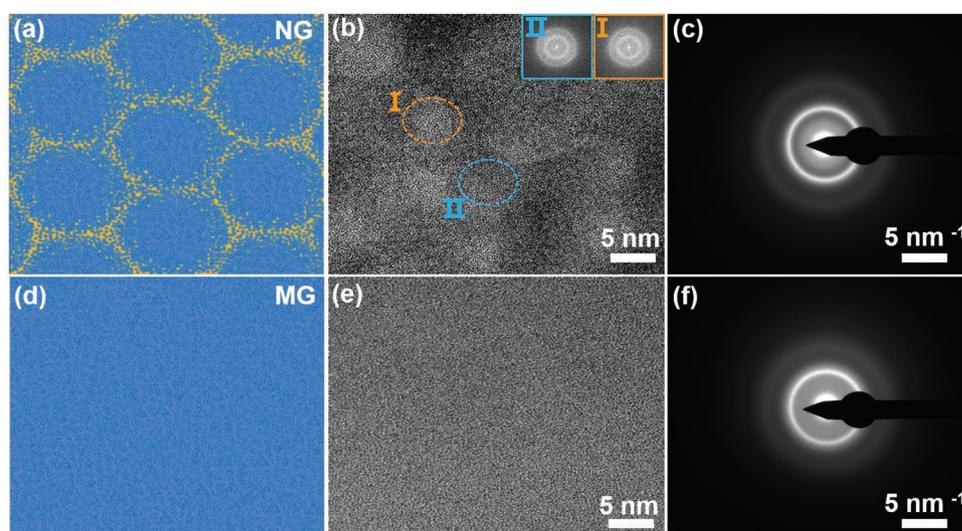
Figure 1. Structural characterization of Ni–P NG and MG. a) The structural model image of NG. b) HRTEM image of NG. The HRTEM image consists of two different regions: a nanoscaled grain region I (in the orange circle) and an interface region II (in the blue circle), and the corresponding FFT patterns of the two regions are shown in the top right. c) Corresponding SAED pattern of (b). d) Structural model image of MG. e) HRTEM image of MG. f) Corresponding SAED pattern of (e).

**ADVANCED
SCIENCE NEWS**

www.advancedsciencenews.com

**ADVANCED
MATERIALS**

www.advmat.de

the results of X-ray diffraction (XRD, Figure S2, Supporting Information). More detailed characterization of the microstructure of Ni–P NGs and MGs have been reported in our previous work.[45]

The differences of the microstructure of Ni–P NG and MG result in different energy states. In order to obtain quantitative information on the energy state of Ni–P NG with the unique grain/interface structure, heat capacity measurements were made using differential scanning calorimetry (DSC) at a heating rate of 20 K min⁻¹ as shown in **Figure 2**a (bottom right). From the heat capacity curves, it is evident that Ni–P NG has a lower crystallization temperature (T_x) of about 588 K compared

with MG (631 K). It indicates that easier trigger crystallization of NG compared with MG, probably due to a lower barrier potential and a higher energy state of NG. For comparison, the rejuvenated MG (RMG) prepared via cryogenic thermal cycling was also measured in the DSC as a reference (temperature programs for the rejuvenation effect are shown in Figure S3, Supporting Information). Rejuvenation is known as a viable method to upgrade the energy state of MG. It is surprising that the RMG indeed has a lower T_x (624 K) than that of MG. However, it is still much higher than the value of 588 K for NG (Figure S4a, Supporting Information), implying a higher energy state of NG than those of both RMG and MG. To further
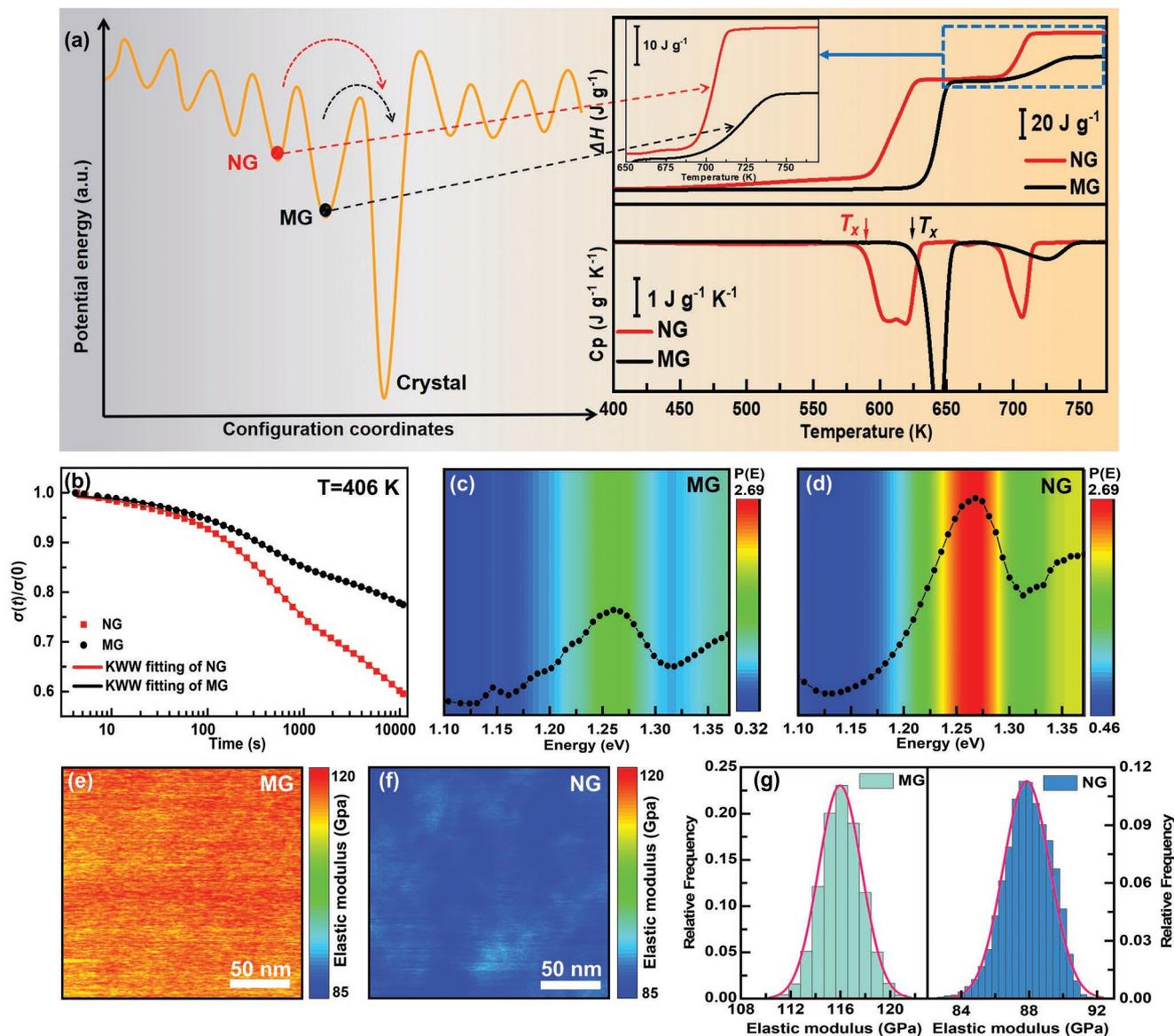
Figure 2. Energy characterization of Ni–P NG and MG. a) The left is a schematic diagram of the potential energy landscape of the NG and MG; the red ball is for NG, and the black ball represents MG. Heat capacity curves of the MG (black line) and NG (red line) are exhibited on the lower right for the heating rate of 20 K min⁻¹. Enthalpy change (ΔH) curves obtained by the integration of the heat capacity curves are displayed on the top right, where the insert is the enlarged image of the ΔH curves. b) The stress-relaxation patterns of NG (red dot) and MG (black dot); the line is the fitting by the KWW equation. c) The distribution of the activation energy spectrum and curve for MG. d) The distribution activation energy spectrum and curve for NG. e) Maps of the surface elastic modulus on MG by AFM. f) Maps of the surface elastic modulus on NG by AFM. g) The corresponding distributions of the surface elastic modulus of MG and NG obtained from (e) and (f).

compare the energy state of NG and MG, the enthalpy change (ΔH) curves are plotted as shown in the Figure 2a (top right) obtained by integrating the heat capacity curves. It is obvious that the ΔH (from 300 to 770 K) of NG is much larger than that of the MG, further demonstrating the higher energy state for NG (the Ni–P NG and MG possess the same crystallization products with identical crystal structure, which indicates the same ground state, Figure S5, Supporting Information). A schematic of the potential energy landscape of the NG and MG, as shown in the left of Figure 2a, indicates that the NG (red dot) is located in a higher energy state than MG (black dot). It is worthy to note that the energy state of NG is even higher than RMG (Figure S4b, Supporting Information), showing the following trend: NG > RMG > MG.

The energy state of MG can be described by the well-established "flow units" model.[46] In this model, the flow units are equivalent to the "defects" in MGs, which are characterized by lower elastic modulus and strength, looser atomic arrangements, higher energy, and higher atomic mobility than other regions in amorphous alloys.[47] Wang et al.[46] confirmed that MG could also produce plastic flow when loading in the elastic region, and found that mechanical relaxation behavior of MG affects the degree of flow. Therefore, stress-relaxation[48] is adapted to express the flow units of the Ni–P NG and MG by dynamical mechanical analyzer (DMA), as shown in Figure 2b. The time dependent stress curves $\sigma(t)/\sigma(0)$ show that the stress decays with increasing time both for NG (red dot) and MG (black dot). It is obvious that Ni–P NG has larger stress decay than that of MG at the same conditions, suggesting that more flow units exist in the NG. Studies show that the stress relaxation behavior of glass can be well used by the extended exponential equation, namely the Kohlrausch–Williams–Watts (KWW) equation,[49] which fits well with the stress relaxation behavior for NG and MG. In addition, we can use the energy barrier to describe the distribution of the flow units in Ni–P NG and MG based on the activation energy spectrum model.[50] In this model, the total available property change of $P(E)$ related to the energy in the relaxation processes are shown in Figure 2c,d. It is noticed that $P(E)$ of NG has a wider distribution at the energy range from 1.20 to 1.36 eV, indicating that more flow units with higher energy barriers are activated during inelastic deformation at temperature of 406 K.

The above characterizations prove that Ni–P NG has higher bulk energy than MG. However, catalytic performance depends much more crucially on the surface conditions. Recently, driving the higher cantilever resonance in a frequency modulated mode with atomic force microscopy (AM-FM) was reported to express the local elastic modulus in structure and the energy-state of MGs by direct measuring the tip–sample interaction stiffness and the set point-independent local elastic modulus with appropriate modeling.[51,52] Figure 2e,f exhibits the elastic modulus mapping of the Ni–P MG and NG measured by AM-FM. As shown in Figure 2g, the NG has a lower elastic modulus than MG. The RMG (Figure S6, Supporting Information) also shows a lower and more inhomogeneous distribution of the elastic modulus compared to MG, which is consistent with previously reported results with its higher energy.[30,51] However, it is interesting that the NG shows much lower elastic modulus distribution than RMG, which indicates

that the highest energy states (the elastic modulus of MG, RMG, and NG are 116, 112, and 88 GPa, respectively, as shown in Figure 2g; Figures S6 and S7, Supporting Information). To avoid possible damage and contamination, the prepared samples were directly used for the atomic force microscopy (AFM) measurements without any further polishing. The details of the surface morphology feature can be seen in Figure S8 (Supporting Information), which shows that all the average surface roughness is less than 0.5 nm, indicating generated modulus almost unaffected by the surface topography by AFM.

The energy state (especially the surface energy) of materials plays a vital role in their catalytic performance. Both the anodic reaction (UOR) and the cathodic reaction (HER) of water splitting were investigated in this work between the Ni–P NG and MG with smooth surface (Figure S9, Supporting Information) as shown in **Figure 3**. UOR is a promising alternative anodic reaction of sluggish OER for water splitting, due to its enhanced efficiency at a far lower potential of 0.37 V[53] (See the Supporting Information for the details of comparison between the UOR and OER, as well as the background of the electrochemical catalytic technique). The UOR performance of polarization curves for two samples are shown in Figure 3a. It is clear that the overpotential of NG is much lower than that of MG during the linear sweep voltammetry (LSV) test, which indicates a significant enhanced UOR catalytic performance of NG. NG also shows a better catalytic performance in the UOR when compared with the high-energy RMG (Figure S10, Supporting Information). Furthermore, the electrochemical impedance spectroscopy (EIS) plots shown in Figure 3b characterize the electrode–electrolyte reactions of Ni–P NG and MG catalysts in the UOR. The equivalent circuit was used to fit the Nyquist plots (the EIS analysis refer to Supporting Information), as inset in Figure 3b.[54,55] The fitted results of EIS plots are shown in Table S1 (Supporting Information). It is obvious that NG exhibits a smaller radius of Nyquist plots with red curve (in Figure 3b), and a smaller value of R_{ct}[54,55] (in Table S1 of the Supporting Information) than MG in the electrolyte, which is conducive to the enhancement of the charge transport and better catalytic effect in the UOR. In addition to the anodic reaction, NG also has a promoted effect on the cathodic reaction, i.e., HER, of water splitting. Figure 3c shows the polarization curves of HER performance for two samples. The NG has a lower overpotential than that of MG during the LSV test, which indicates the improved HER catalytic performance. In addition, the EIS plots in Figure 3d also exhibit a smaller radius of Nyquist plots with NG (red curve), further demonstrating the better catalytic effect in the HER. To study the discrepancy of surface composition and electronic states of Ni–P NG and MG, XPS results are shown in Figure 3e–g. The survey spectra containing signals of Ni, P, C, and O elements are summarized in Figure S11 (Supporting Information). High-resolution spectra for Ni 2p of NG and MG are presented in Figure 3e; the binding energy at 861.59 eV (NG) and 861.00 eV (MG) can be assigned to the satellite peaks. In addition, the peaks at 853.12 eV ($Ni^{\delta+}$ $2p_{3/2}$ for NG) and 853.15 eV ($Ni^{\delta+}$ $2p_{3/2}$ for MG) are very close to that of zero valence state Ni,[56,57] indicating partial metallic and partial positive ionic features for Ni atoms ($0 < \delta < 2$) in Ni–P.[5,58] Interestingly, it turns out that the Ni^{2+} $2p_{3/2}$ binding energy shifts 0.2 eV from 856.16 (MG) to 856.36 eV (NG). The
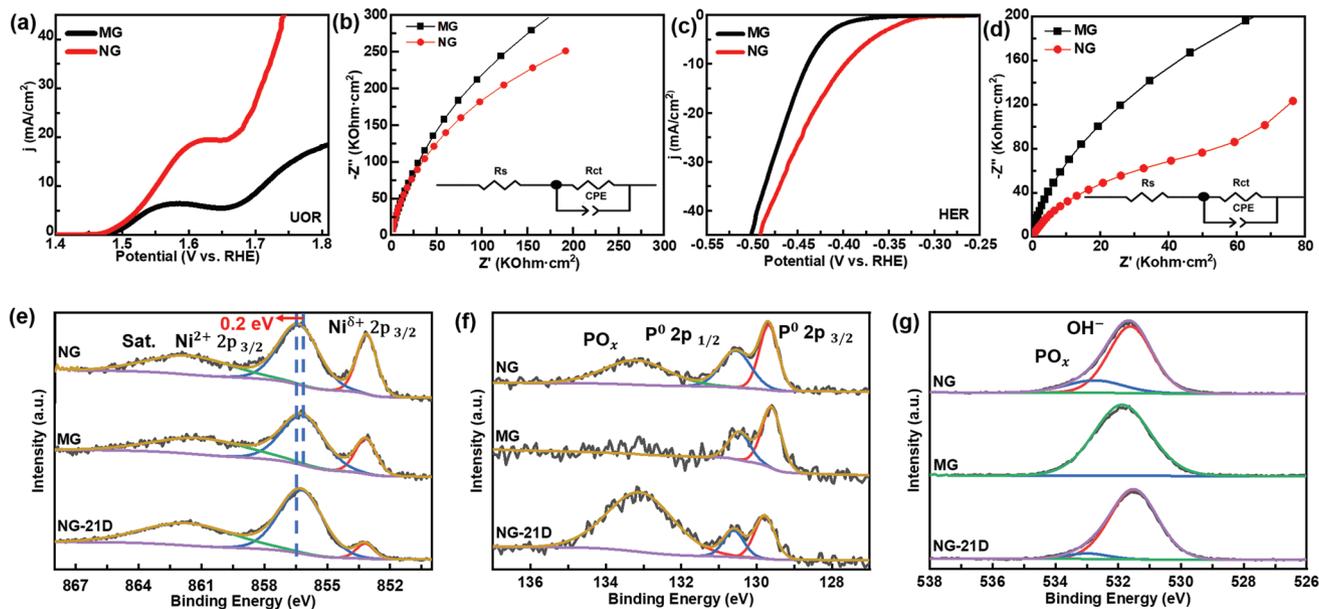
Figure 3. Catalytic performance and the electronic states on the electrode surface of the NG and MG. a) Polarization curves of NG (red line) and MG (black line) catalysts in the UOR. b) EIS of the NG and MG catalysts in the UOR. The inset shows a simplified equivalent circuit for EIS data fitting. c) Polarization curves of NG and MG catalysts in the HER. d) EIS of the NG and MG catalysts in the HER. The inset shows a simplified equivalent circuit for EIS data fitting. e) High-resolution XPS spectra of Ni 2p of NG, MG, and NG-21D. f) High-resolution XPS spectra of P 2p of NG, MG, and NG-21D. g) High-resolution XPS spectra of O 1s of NG, MG, and NG-21D.

peaks at 130.55 eV (NG), 129.68 eV (NG), 130.46 eV (MG), and 129.60 eV (MG) are in good agreement with the binding energy of P $2p_{1/2}$ and P $2p_{3/2}$ (Figure 3f), respectively. Comparing with MG, NG shows a significantly increased amount of phosphates at the binding energy of 133.20 eV (in Figure 3f, where there is no obvious peak shown for MG of PO_x) and 532.74 eV (Figure 3g), where the phosphates can act as a proton transport mediator at catalyst surface.[59] In addition, the hydroxy peaks of 531.61 eV (NG, Figure 3g) and 531.87 eV (MG, Figure 3g) at the catalyst surface are usually considered as the active sites for catalytic performance.[60] In summary, the binding energy of the Ni^{2+} for NG is higher than that of MG, indicating that the metallic element (Ni) formed a solution that possesses a higher potential energy, resulting in a lower energy barrier during the catalytic processes.

The intrinsic catalytic performance of Ni–P NG for water splitting is proven to be substantially better than MG. Leveraging the excellent intrinsic activity with formulations that provide higher surface area could lead to further improvements in overall catalytic efficiency of NG. Thus, the Ni–P NGs were immersed in the NaCl solution (3.5 wt%) at the room temperature over different times (such as 7 days (named as NG-7D), 14 days (NG-14D), 21 days (NG-21D, MG-21D), and 28 days (NG-28D)) for modification of the surface morphology, respectively.

The anodic reactions of water splitting, both OER and UOR, were conducted to highlight the catalytic performance of these modified Ni–P NGs. **Figure 4**a shows representative polarization curves of five NGs electrodes in the OER. NG-14D and NG-21D exhibit very low potential of 1.56 and 1.54 V (vs RHE), respectively, at current density of 10 mA cm^{-2} in 1 M KOH, which are much smaller than that of bare NG, as well as those of most reported transitional metal-based OER catalyst. To verify their superior catalytic performance, the UOR was further studied on NG-14D and NG-21D, as well as NG for comparison. Figure 4b exhibits the LSV results for UOR by using the NG (as the reference sample), NG-14D and NG-21D as electrocatalysts. NG and NG-14D exhibit a strong anodic peak corresponding to oxidation of urea followed by a decrease in the current density and the oxidation of OH^{-} occurs at higher potentials. For NG-21D, only a tail like shape LSV corresponding to urea oxidation was observed, due to the oxidation of OH^{-} unhappen within the test voltage range. To our surprise, comparing with NG and NG-14D, NG-21D demonstrates a much better UOR effect with a lower potential at 1.36 V versus RHE to attain a current density of 10 mA cm^{-2}. The C_{dl} (the details can be seen in Supporting Information) plots shown in Figure 4c indicate that the NG-21D has a larger value of 0.061 mF cm^{-2} with smaller pore sizes (CV plots are shown in Figure S12, Supporting Information). This observation indicates that the NG-21D with promoted catalytic effect possesses larger electrochemical active surface areas. To weigh material intrinsic activity, electrochemically active surface area (ECSA) and corresponding ECSA normalized current density of NG and NG-21D were calculated based on C_{dl}. As shown in Figure S13 (Supporting Information), the NG-21D exhibits much better catalytic performance than NG, as indicated by higher ECSA normalized current density. Moreover, Tafel curves of the NG, NG-14D and NG-21D catalyst are summarized in Figure 4d with different slope of plots, 53 mV dec^{-1} for NG, 35 mV dec^{-1} for NG-14D, and 13 mV dec^{-1} for NG-21D, respectively. The accuracy of Tafel slope was confirmed by quasi-steady-state measurement (Figures S14 and S15, Supporting Information). As a result, the lower slope of NG-21D reveals a favorable reaction kinetic for UOR. It can be observed that the NG-21D has the smallest diameter of semicircles and a lower

**ADVANCED
SCIENCE NEWS**
www.advancedsciencenews.com

**ADVANCED
MATERIALS**
www.advmat.de
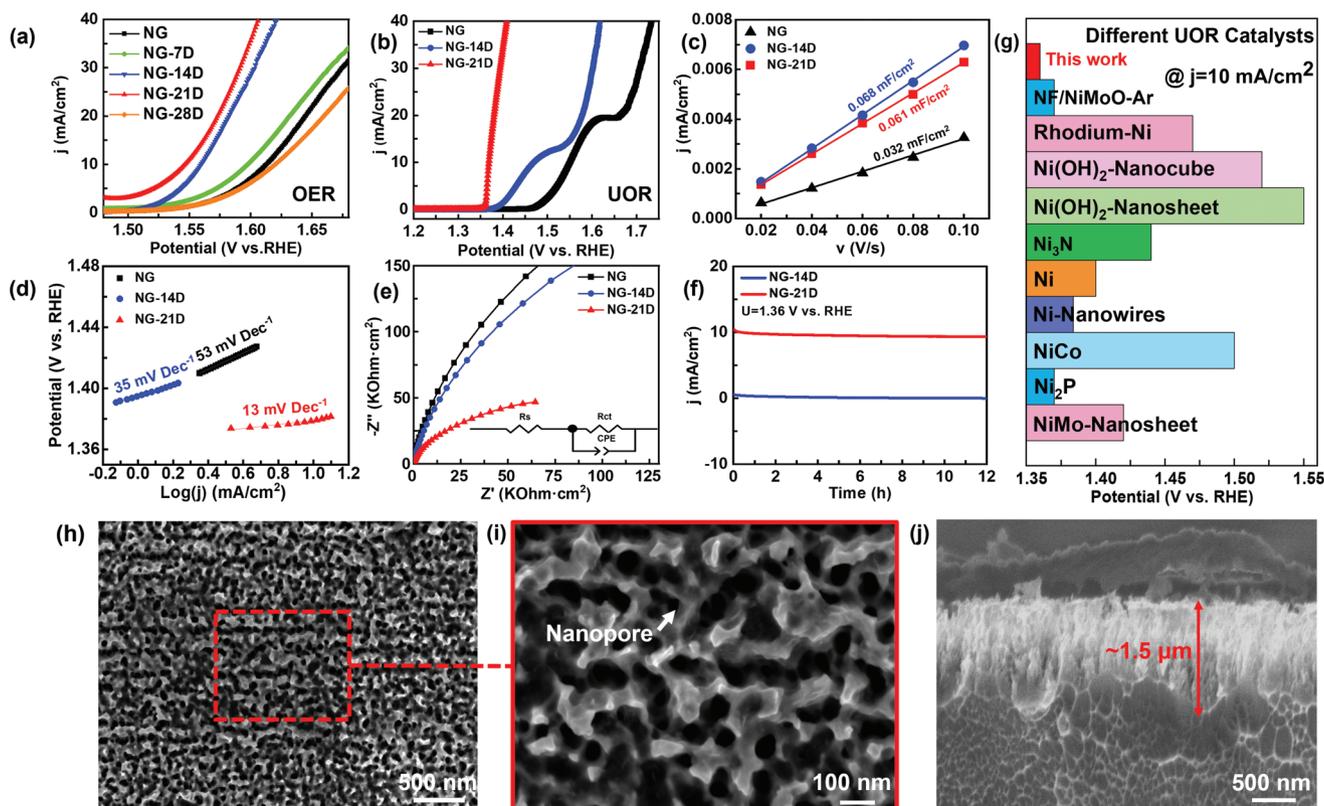
Figure 4. The anodic reaction performance of Ni–P NG catalysts and morphology of NG-21D. a) Polarization curves of NG, NG-7D, NG-14D, NG-21D, and NG-28D catalysts in the OER. b) Polarization curves of the NG, NG-14D, and NG-21D catalysts in the UOR. c) Extraction of the C_{dl} from three Ni–P electrodes, NG, NG-14D and NG-21D in the UOR. d) Tafel curves of the NG, NG-14D, and NG-21D catalysts in the UOR. e) EIS of the NG, NG-14D, and NG-21D catalysts in the UOR. The inset shows a simplified equivalent circuit for EIS data fitting. f) The chronoamperometric test of NG-14D and NG-21D for 12 h at the potential of 1.36 V (vs RHE) in the UOR. g) The statistics of potential vs RHE @ $j = 10$ mA cm^{-2} for different Ni-based catalysts on the UOR; the red bar is for this work. h) The surface morphology image of NG-21D by SEM. i) HRSEM image from the red region in image 4 h of NG-21D. The black regions represent the nanopores. j) The cross-section SEM image of NG-21D.

value of R_{ct} (Figure 4e) among the comparison with the samples of NG and NG-14D, corresponding to a better and faster kinetics in the UOR (the values of R_{ct} by fitting the EIS curves were listed in Table S1, Supporting Information). To investigate the electrochemical catalysis stability of NG-21D, UOR in 1 M KOH solution at a constant potential of 1.36 V versus RHE for 12 h was conducted, as shown in Figure 4f. Further, NG-14D also tested for comparative study. NG-21D exhibits an excellent stability without obvious current density deterioration. In addition, the current density of NG-21D is much larger than that of NG-14D, further confirming the better catalytic performance of NG-21D. Figure 4g shows the potential versus RHE @ 10 mA cm^{-2} of different Ni-based catalysts. It is noteworthy that the present NG-21D catalyst exhibits the lowest potential among the other Ni-based catalysts (marked as the red bar), which clearly indicates the best catalytic performance.

To further study the surface composition and electronic states of modified NGs with the most excellent catalytic performance in the UOR, XPS measurements were carried out with NG-21D and others three samples. The survey spectra containing signals of Ni, P, C, and O elements of NG-21D are shown in Figure S11 (Supporting Information). The high-resolution spectrum for Ni 2p of NG-21D is presented in Figure 3e (with others high-resolution spectra of NG-7D, NG-14D, and

NG-28D can be seen in Figure S16, Supporting Information). The NG-21D shows the Ni^{2+} 2p$_{3/2}$ peak at the binding energy of 856.25 eV. The binding energy at 853.19 eV of NG-21D can be assigned to Ni$^{\delta+}$ 2p$_{3/2}$ together with the satellite peaks of 861.68 eV (NG-21D, Figure 3e). It is obvious that the binding energy of Ni of NG-21D blue shifts 0.2 eV compares with that of NG, which suggests that the etching process promotes the atomic diffusion rate and give rise to an atomic rearrangement.[61] For P 2p (shown in Figure 3f) of NG-21D, the two subspectra at 130.61 and 129.79 eV are assigned to P 2p$_{1/2}$ and P 2p$_{3/2}$ and the peak at 133.10 eV is assigned to oxidized species (PO$_x$) in Figure 3g.[62] Compared with the NG, it can be clearly seen from Figure 3f that there is an obvious enhanced peak centered at 133.10 eV of NG-21D, where the peaks belong to PO$_x$[58] indicating that the content of PO$_x$ has increased after immersion in the NaCl solution. It is well accepted that the presence of PO$_x$ on an electrocatalyst surface can make essential contributions to accelerate the water dissociation step.[63] For O 1s of NG-21D (Figure 3g), the XPS spectrum result of the binding energy at 533.00 eV can be assigned to PO$_x$ and 531.50 eV could be OH$^-$, which corresponds well to the XPS results of P 2p in Figure 3f.

In order to gain insights in the nature of the NGs catalyst, XRD of five samples (NG, NG-7D, NG-14D, NG-21D, and

NG-28D) were performed to probe the glassy state of the Ni–P NGs. These results are shown in Figure S17 (Supporting Information). All the Ni–P samples exhibit board diffraction peaks between 40° and 50°, providing proof of the amorphous structure. Since a catalytic reaction is a surface-mediated process, the microstructure characteristics of NG-21D were investigated by SEM. The images of NG-21D, as shown in Figure 4h, reveal substantial and homogeneous corrosion marks on the surface. Furthermore, the SEM images of the other samples (MG-21D, NG-7D, NG-14D, and NG-28D) are summarized in Figure S18 (Supporting Information). These samples exhibit different degrees of corrosion of NG after soaked in the NaCl solution, while the MG-21D does not show an obvious corrosion. In order to figure out the detailed morphology of the surface of NG-21D, as shown in Figure 4i, the evenly distributed 3D nanoporous structure on the surface of this sample after immersing in the NaCl solution (3.5 wt %) 21 days can be observed clearly. In Figure 4j, a cross-section image of the distributed 3D nanochannel structure is shown, which exhibits a special honeycomb structure with the depth of ≈1.5 µm. Combined with the images in Figure 4i,j, it is concluded that the structure in the corroded samples is a honeycomb-like nanoporous NG, which is consistent with the structure prepared by Luo et al.,[64] where a honeycomb-like porous MG prepared by subsurface tunnel etching in NaCl solution indicates characteristic micrometer scale channels and nanometer size amorphous sidewalls on the MG substrate. In addition, the element distribution on the surface of the samples was explored using the EDS equipment in the SEM and showed in Figure S19 (Supporting Information). The EDS mapping in Figure S19 (Supporting Information) suggests that the Ni and P elements are evenly distributed on the surface of NG-21D and there is no obvious segregation phenomenon. Only a small amount of O element on the surface corresponding to the results of XPS in Figure 3g is observed. Furthermore, some characterizations of XRD and SEM of NG, NG-14D, and NG-21D after UOR were also supplemented in Supporting Information. According to the XRD results after the reaction (Figure S20, Supporting Information), all the samples still maintained a good amorphous state. And SEM results (Figure S21, Supporting Information) show that a serious oxide layer is generated on the surface of NG-14D after UOR, resulting in the covering of porous structure, which will greatly reduce its catalytic performance. However, NG-21D produces only a small part of oxide layer, contributing to the better the catalytic performance and stability of the sample.

The present work demonstrates that the energy state of the Ni–P MG is highly upgraded when it transformed into a NG structure. NG has a heterogeneous microstructure compared to MG, and contains more high-energy flow units as measured by stress-relaxation (Figure 2b–d). NG possesses a lower elastic modulus compared to MG and RMG as measured by AM-FM measurement (Figure 2e–g), indicating the highest surface energy state of NG. Moreover, in our previous work, it was illustrated by β-relaxation that a correlation between the heterogeneous microstructure and the energy state of NG exists.[34] It has been demonstrated that the intensity of the β-relaxation peak is attenuated with the microstructure homogenization of NG by heat treatment. It should be noticed that the attenuation of intensity of the β-relaxation peak indicates a reduction

of energy. Thus, it is speculated that the high-energy of the NG is related to the unique structure with more flow units compared to the MG.

It is well accepted that the catalytic performance will benefit from the high energy states. Particularly, the higher surface energy will be equivalent to a higher activity, derived from the larger number of low-coordinated sites on a catalyst surface.[14–18] Catalytic active sites are usually composed of a few low-coordinated atoms on steps, edges and kinks.[19–21] Therefore, NG with high energy exhibits a promoted catalytic performance compared to MG, such as in the UOR and HER. Furthermore, NG has a smaller charge transfer resistance than MG in the electrolyte (Figure 3b,d and Table S1, Supporting Information), which is conducive to the rapid transfer of electrons due to the surface high energy, then resulting in the enhancement of the kinetics of the catalytic reaction. Consequently, NG displays a better catalytic effect than MG due to its highly upgraded energy state arising from the unique heterogeneous microstructure.

In addition, an excellent performance of NG-21D was demonstrated by tuning the structure by means of immersion in a NaCl solution (3.5 wt%), thus forming a unique honeycomb-like porous structure with an average length of the tunnels ≈1.5 µm. To identify the differences between NG and MG in the formation of the honeycomb-like porous structure, a MG was also etched (Figure S18, Supporting Information). It is surprising that only the NGs form the nanoporous structure, which indicates that the different behavior is related to the heterogeneous microstructure with low-density (high-energy) interface region, as shown in Figure 2g and Figure S7 (Supporting Information). Generally, porous structures promote the close contact between the electrode, catalyst and electrolyte, which ensures the rapid transfer of charge and improve the current of the oxidation reaction,[7,65] thus reducing the overpotential in the UOR. Meanwhile, the porous structure increases the active surface area with high-energy and provides more active sites. What is more, the XPS result (Figure 3f,g) shows that the PO_x content on the surface of NG-21D has increased after immersion in sodium chloride solution for 21 days, suggesting the formation of a passivation film of P oxide, which is speculated to play a synergistic role in promoting the catalytic reaction and be conducive to the long-term stable existence of the sample in the electrolyte. As a result, NG-21D has a good stability in the 12-h electrochemical test (shown in Figure 4f). In other words, the outstanding catalytic effect of NG-21D is deriving from both the high energy state and the unique honeycomb-like porous structure.

3. Conclusion

Ni–P NG was successfully prepared and its extremely high energy state was verified in comparison to MG and even RMG. The high energy state (including bulk and surface energy) of NG is attributed to the unique heterogeneous microstructure, which significantly enhances the catalytic performance in water-splitting, including UOR, OER, and HER. Moreover, NGs with heterogeneous microstructure are a perfect precursor material for the fabrication of unique honey-like nanoporous

structure, which display a superior catalytic performance in the UOR. The present work provides a facile and universal strategy to synthesize extremely high-energy MGs by nanostructurization and thus offers a new idea for further studies of efficient catalytic materials. Overall, the combination of exceptional catalytic activity by combination of internal structural defects in NG and the formation of nanoporous structures offers new applications in the field of clean energy.

Supporting Information

Supporting Information is available from the Wiley Online Library or from the author.

Conflict of Interest

The authors declare no conflict of interest.

Data Availability Statement

The data that support the findings of this study are available from the corresponding author upon reasonable request.

[1] H. B. Yu, M. Tylinski, A. Guiseppi-Elie, M. Ediger, R. Richert, *Phys. Rev. Lett.* **2015**, *115*, 185501.
[2] J. Ma, C. Yang, X. Liu, B. Shang, Y. Yang, *Sci. Adv.* **2019**, *5*, eaax7256.
[3] H. Wagner, D. Bedorf, S. Küchemann, M. Schwabe, B. Zhang, W. Arnold, K. Samwer, *Nat. Mater.* **2011**, *10*, 439.
[4] S. A. Baranov, V. S. Larin, A. V. Torcunov, *Crystals* **2017**, *7*, 136.
[5] X. Guo, W. Zhang, R. Shi, H. Zhu, C. Qian, H. Yang, J. Zhang, A. Yuan, Y. Zhou, *ChemElectroChem* **2019**, *6*, 3071.
[6] X. Yan, J. Sun, Y. Wang, J. Yang, *Mol. Catal.* **2006**, *252*, 17.
[7] Y. Jin, G. Xi, R. Li, Z. A. Li, X. B. Chen, T. Zhang, *J. Alloys Compd.* **2021**, *852*, 156876.

[8] S. Chen, G. Yang, S. Luo, S. Yin, J. Jia, Z. Li, S. Gao, K. F. Yao, Y. Shao, *J. Mater. Chem. A* **2017**, *5*, 14230.
[9] Z. Jia, W. C. Zhang, W. M. Wang, D. Habibi, L. C. Zhang, *Appl. Catal., B* **2016**, *192*, 46.
[10] S. Chen, M. Li, X. Ma, M. Zhou, D. Wang, M. Yan, Z. Li, K. Yao, *Chemosphere* **2021**, *264*, 128392.
[11] A. Simonov, A. L. Goodwin, *Nat. Rev. Chem.* **2020**, *4*, 657.
[12] G. Prieto, S. Beijer, M. L. Smith, H. Ming, Y. Au, Z. Wang, D. A. Bruce, K. D. Jong, J. J. Spivey, P. D. Jongh, *Angew. Chem., Int. Ed.* **2014**, *126*, 6515.
[13] W. X. Huang, W. Xue, *Phys. Chem. Chem. Phys.* **2019**, *21*, 523.
[14] N. Tian, Z. Y. Zhou, S. G. Sun, *J. Phys. Chem. C* **2008**, *112*, 19801.
[15] T. Sheng, Y. F. Xu, Y. X. Jiang, L. Huang, N. Tian, Z. Y. Zhou, I. Broadwell, S. G. Sun, *Acc. Chem. Res.* **2016**, *49*, 2569.
[16] H. Zhang, M. Jin, Y. Xiong, B. Lim, Y. Xia, *Acc. Chem. Res.* **2013**, *46*, 1783.
[17] N. S. Porter, H. Wu, Z. Quan, J. Fang, *Acc. Chem. Res.* **2013**, *46*, 1867.
[18] Q. Chen, Y. Jia, S. Xie, Z. Xie, *Chem. Soc. Rev.* **2016**, *45*, 3207.
[19] N. P. Lebedeva, A. Rodes, J. M. Feliu, M. Koper, R. Santen, *J. Phys. Chem. B* **2002**, *106*, 9863.
[20] Q. S. Chen, A. Berna, V. Climent, S. G. Sun, J. M. Feliu, *J. Phys. Chem.* **2010**, *12*, 11407.
[21] S. L. Bernasek, G. A. Somorjai, *Surf. Sci.* **1974**, *48*, 204.
[22] P. G. Debenedetti, F. H. Stillinger, *Nature* **2001**, *410*, 259.
[23] J. Wang, L. Han, B. Huang, Q. Shao, H. L. Xin, X. Huang, *Nat. Commun.* **2019**, *10*, 5692.
[24] G. Chen, Y. Zhu, H. M. Chen, Z. Hu, S. F. Hung, N. Ma, J. Dai, H. J. Lin, C. T. Chen, W. Zhou, *Adv. Mater.* **2019**, *31*, 1900883.
[25] X. Zhang, Z. Luo, P. Yu, Y. Cai, Y. Du, D. Wu, S. Gao, C. Tan, Z. Li, M. Ren, *Nat. Catal.* **2018**, *1*, 460.
[26] Y. H. Sun, A. Concustell, A. L. Greer, *Nat. Rev. Mater.* **2016**, *1*, 16039.
[27] W. Song, X. Meng, Y. Wu, D. Cao, H. Wang, X. Liu, X. Wang, Z. Lu, *Sci. Bull.* **2018**, *63*, 840.
[28] J. Ketkaew, Y. Rui, W. Hui, D. Kuldinow, J. Schroers, *Acta Mater.* **2019**, *184*, 100.
[29] H. Lou, Z. Zeng, F. Zhang, S. Chen, Q. Zeng, *Nat. Commun.* **2020**, *11*, 314.
[30] J. Pan, Y. X. Wang, Q. Guo, D. Zhang, A. L. Greer, Y. Li, *Nat. Commun.* **2018**, *9*, 560.
[31] C. Guo, Y. Fang, B. Wu, S. Lan, G. Peng, X.-l. Wang, H. Hahn, H. Gleiter, T. Feng, *Mater. Res. Lett.* **2016**, *5*, 293.
[32] H. Gleiter, *Acta Mater.* **2008**, *56*, 5875.
[33] T. Feng, H. Hahn, H. Gleiter, *Acta Phys. Sin.* **2017**, *66*, 176110.
[34] Q. Yang, C. Q. Pei, H. B. Yu, T. Feng, *Nano Lett.* **2021**, *21*, 6051.
[35] N. Chen, R. Frank, N. Asao, D. V. Louzguineluzgin, P. Sharma, J. Q. Wang, G. Q. Xie, Y. Ishikawa, N. Hatakeyama, Y. C. Lin, *Acta Mater.* **2011**, *59*, 6433.
[36] C. Zequine, F. Wang, X. Li, D. Guragain, S. R. Mishra, K. Siam, P. Kahol, R. Gupta, *Appl. Sci.* **2019**, *9*, 793.
[37] B. J. Zhu, Z. B. Liang, R. Q. Zou, *Small* **2020**, 16, 1906133.
[38] R. P. Forslund, J. T. Mefford, W. G. Hardin, C. T. Alexander, K. P. Johnston, K. J. Stevenson, *ACS Catal.* **2016**, *6*, 5044.
[39] J. Zhang, T. Wang, P. Liu, Z. Liao, S. Liu, X. Zhuang, M. Chen, E. Zschech, X. Feng, *Nat. Commun.* **2017**, *8*, 15437.
[40] M. Ma, F. Qu, X. Ji, D. Liu, S. Hao, G. Du, A. M. Asiri, Y. Yao, L. Chen, X. Sun, *Small* **2017**, *13*, 1700394.
[41] Y. Y. Chen, Y. Zhang, X. Zhang, T. Tang, H. Luo, S. Niu, Z. H. Dai, L. J. Wan, J. S. Hu, *Adv. Mater.* **2017**, *29*, 1703311.
[42] J. Greeley, T. F. Jaramillo, J. Bonde, I. Chorkendorff, J. K. Nørskov, *Nat. Mater.* **2006**, *5*, 909.
[43] Y. Jiao, Y. Zheng, M. Jaroniec, S. Z. Qiao, *Chem. Soc. Rev.* **2015**, *46*, 2060.
[44] D. Merki, X. Hu, *Energy Environ. Sci.* **2011**, *4*, 3878.

[45] S. Lan, C. Guo, W. Zhou, Y. Ren, J. Almer, C. Q. Pei, H. Hahn, C. T. Liu, T. Feng, X. L. Wang, *Commun. Phys.* **2019**, *2*, 117.

[46] Z. Wang, P. Wen, L. S. Huo, H. Y. Bai, W. H. Wang, *Appl. Phys. Lett.* **2012**, *101*, 121906.

[47] L. S. Huo, J. F. Zeng, W. H. Wang, C. T. Liu, Y. Yang, *Acta Mater.* **2013**, *61*, 4329.

[48] C. Pei, R. Zhao, Y. Fang, S. Wu, T. Feng, *J. Alloys Compd.* **2020**, *836*, 155506.

[49] F. Alvarez, A. Alegría, J. Colmenero, *Phys. Rev. B* **1993**, *47*, 125.

[50] M. Gibbs, J. E. Evetts, J. A. Leake, *J. Mater. Sci.* **1983**, *18*, 278.

[51] M. Gao, J. H. Perepezko, *Nano Lett.* **2020**, *20*, 7558.

[52] M. Kocun, A. Labuda, W. Meinhold, I. Revenko, R. Proksch, *ACS Nano* **2017**, *11*, 10097.

[53] Y. Tong, P. Chen, M. Zhang, T. Zhou, L. Zhang, W. Chu, C. Wu, Y. Xie, *ACS Catal.* **2017**, *8*, 1.

[54] H. Ashassi-Sorkhabi, M. Es, *Corros. Sci.* **2013**, *77*, 185.

[55] G. Zhao, Y. Zou, S. Jinwen, K. Matsuda, Z. Zou, J. Chen, *Intermetallics* **2016**, *11*, 140.

[56] A. N. Mansour, *Surf. Sci. Spectra* **1994**, *3*, 231.

[57] K. S. Kim, N. Winograd, *Surf. Sci. Spectra* **1974**, *43*, 625.

[58] Y. Pan, Y. Liu, J. Zhao, K. Yang, J. Liang, D. Liu, W. Hu, D. Liu, Y. Liu, C. Liu, *J. Mater. Chem. A* **2015**, *3*, 1656.

[59] R. Ye, P. Del Angel-Vicente, Y. Liu, M. J. Arellano-Jimenez, Z. Peng, T. Wang, Y. Li, B. I. Yakobson, S. H. Wei, M. J. Yacaman, *Adv. Mater.* **2016**, *28*, 1427.

[60] L. Trotochaud, S. L. Young, J. K. Ranney, S. W. Boettcher, *J. Am. Chem. Soc.* **2014**, *136*, 6744.

[61] R. Li, X. Liu, R. Wu, J. Wang, Z. Li, K. Chan, H. Wang, Y. Wu, Z. Lu, *Adv. Mater.* **2019**, *31*, 1904989.

[62] S. Wang, Z. Li, L. Xiao, C. Li, R. Zhang, Y. Zhang, H. Zhu, *Nano Res.* **2017**, *10*, 415.

[63] D. Zhu, L. Wang, M. Qiao, J. Liu, *Chem. Commun.* **2020**, *56*, 7159.

[64] X. Luo, M. Meng, R. Li, Z. Li, T. Zhang, *Mater. Des.* **2020**, *196*, 109109.

[65] G. Xi, L. Zuo, X. Li, Y. Jin, R. Li, T. Zhang, *J. Mater. Sci. Technol.* **2021**, *70*, 197.